Room-temperature–low-pressure-operating high-energy lithium metal batteries employing garnet-type solid electrolytes and anode interlayers

Ju-Sik Kim (jusik.kim@samsung.com)
Samsung Advanced Institute of Technology https://orcid.org/0000-0002-5204-3518
Gabin Yoon
Samsung Advanced Institute of Technology https://orcid.org/0000-0001-7669-6225
Sewon Kim
Samsung Advanced Institute of Technology https://orcid.org/0000-0002-3886-8898
Shoichi Sugata
Samsung Electronics
Nobuyoshi Yashiro
Samsung Electronics
Shinya Suzuki
Samsung Electronics
Myung-Jin Lee
Samsung Advanced Institute of Technology
Ryoung-Hee Kim
Samsung Advanced Institute of Technology
Michael Badding
Corning Incorporated
Zhen Song
Corning Incorporated
JaeMyung Chang
Corning Incorporated
Dongmin Im
Samsung Advanced Institute of Technology (SAIT), Samsung Electronics Co. Ltd.
https://orcid.org/0000-0003-2788-0477

Article

Keywords: Garnet solid electrolytes, Li metal batteries, anode interlayers, Li-metal/Garnet electrolyte interface

Posted Date: April 27th, 2022

DOI: https://doi.org/10.21203/rs.3.rs-1551346/v1

Version of Record: A version of this preprint was published at Nature Communications on February 11th, 2023. See the published version at https://doi.org/10.1038/s41467-023-36401-7.

Abstract

Lithium metal batteries (LMBs) are considered the most promising next-generation battery system because of their high energy density and safety. Significant research effort has been devoted to developing more stable and energy-dense LMBs than the state-of-the-art Li-ion batteries. However, the LMB performance remains unsatisfactory for commercialization, primarily owing to the inability of solid electrolytes to block Li dendrite propagation. Herein, we demonstrate highly stable LMB employing garnet-type oxide electrolyte by introducing a carbon-based interlayer with careful interface engineering. We theoretically and experimentally demonstrate that our design effectively regulated Li deposition away from the solid electrolyte, preventing dendrite penetration. We further demonstrated that the interface condition between the interlayer and solid electrolyte is critical and present an effective strategy to achieve an optimal interface. Overall, our garnet-type oxide-based LMB exhibited a high energy density of ~ 680 Wh/L for over 800 cycles at room temperature without using external pressure.

Introduction

As carbon neutrality is becoming a pressing issue for sustainability, the development of lithium-ion batteries (LIBs), a key technology for electric vehicles and electric storage systems for smart grids, has attracted significant interest. To push the limits of LIBs, all-solid-state Li batteries have recently drawn considerable attention owing to their superior energy density and safety that can potentially enhance LIB performance[1–4]. In particular, the use of Li metal as an anode can considerably increase energy density; the non-flammable feature of solid electrolytes can prevent potential fire hazards caused by thermal shock or short-circuit, even in high-capacity battery cells.

Garnet-structured oxide solid electrolytes ($Li_7La_3Zr_2O_{12}$, LLZO archetype) have been widely used as a solid electrolyte material owing to their high ionic conductivity (~ 1 mS/cm @ 25°C) and excellent reduction stability to Li metal[5–10]. However, there are plenty of obstacles preventing its practical realization, including dendrite penetration through solid electrolytes[11–15]. Several approaches, such as coating organic/inorganic layers to protect interface and increase the wettability, modifying the interfacial nanostructure to reduce the local current density, and chemical treatment to remove native layers at the electrolyte surface, have been attempted to alleviate this issue[16–20]. Efforts to enhance Li wetting using molten Li or metallic coating materials could effectively reduce the initial interfacial resistance, but the long-term cycle performance of full cells was not satisfactory, and the critical current density was predominantly under 1 mA/cm^2, which is lower than the practical operating condition. Porous-dense-porous trilayer structure of garnet could block dendrites under a high current density (~ 10 mA/cm^2) by increasing the interface area, but the effect was diminished in full-cell operation[21]. It was also demonstrated that the acid treatment on garnet considerably increased dendrite resistance by simultaneously removing the native layer and enlarging the interface area, but the long-term cycling was demonstrated only at elevated temperatures[22].

Introducing a carbon-based interlayer between the solid electrolyte and anode has recently been proven effective at suppressing dendrite propagation. Using a Ag–C composite interlayer and sulfide solid electrolyte, a high reversibility for ~ 1000 cycles was demonstrated in a pouch cell with a high current density of 3.4 mA/cm^2[23]. It was demonstrated that a crucial role of the interlayer is to guide the Li deposition/stripping occurring between the interlayer and current collector. Consequently, the direct contact between Li metal and the solid electrolyte, which commonly leads to non-uniform current distribution, and the resulting penetration of Li dendrites through the solid electrolyte, can be effectively prevented during charge/discharge cycles. However, the mechanism of the Li deposition site regulation remains unclear, because the mixed ionic-electronic conducting nature of the Ag–C composite would promote Li deposition/stripping at the interface between the solid electrolyte and Ag–C composite.

In this study, we first explored the thermodynamic origin of preferable Li deposition toward current collector in the presence of carbon-based interlayer. We then incorporated a Ag–C composite interlayer onto Ta-doped LLZO (LLZTO) using a nanometer-thick Ag layer sputtered at the LLZTO surface. This design enabled highly reversible Li deposition between LLZTO and the current collector, realizing a high energy density of 680 Wh/L for 800 cycles at room temperature (25°C) without external pressure.

Methods

Materials

LLZTO ($Li_{6.4}La_3Zr_{1.7}Ta_{0.3}O_{12}$) powder was synthesized using a solid-state reaction method with a precursor mixture of Li_2CO_3 (> 99.0%, ChemPoint), La_2O_3 (98.6%, MolyCorp), Ta_2O_5 (99.99%, Sigma Aldrich), and ZrO_2 (98%, Zircoa Inc.). The mixed powders were calcined in air at 950°C for 5 h followed by 1,200°C for 5 h to form the LLZTO powder. The calcined powders were then ball-milled with zirconia balls for 10 min at 300 rpm using a planetary mill (Pulverisette 7, Fritsch, Germany). Ball milling was repeated 12 times at 5-min intervals.

To fabricate a dense pellet, the LLZTO powders (100g) were hot-pressed into a graphite die at 3kpsi, followed by sintering at 1,100°C for 2 h in an argon atmosphere at the heating rate of 300°C/min. The relative density of the pellet was estimated to be > 98% with respect to the theoretical density of LLZTO calculated from the X-ray diffraction data. The pellets were cut into 14-mm-diameter discs with 360-μm-thickness using a laser cutter. Next, they were cleaned via ultrasonic cleaning in hexane for 10 min and heat-treated at 800°C for 1 h in dry air. Finally, the pellet surface was polished to a thickness of ~ 350 μm using polishing machines (LaboForce-3, Struers).

A thin electrolyte film was prepared via tape casting. LLZTO powder was added to a mixed solvent of toluene and isopropanol, and was then mixed for approximately 1 h. Fish oil, polyvinyl butyral, and butyl benzyl phthalate were added to the slurry as a binder and dispersant. The resulting slurry was removed as a thin film on a Mylar sheet, and then dried at 120°C for 1 h. The green tape was sintered at 1100°C for 2 h.

Acid treatment was performed for cleaning the LLZTO surface by simply immersing the discs into a 1 M HCl solution (in distilled water) for 20 min at a weight ratio of 1:10 (pellet:acid solution) at room temperature. To prevent the local variation in concentration in the acid solution due to the released Li or prevent the close contact of the electrolyte to the container, the container was rolled at approximately 60 rpm during protonation. We then removed the solution, washed the discs with ethanol, and dried them in a dry room.

Fabrication of electrochemical cells

We employed a hybrid electrolyte cell in all full cell evaluations. In the hybrid cells, an ionic liquid and a solid oxide electrolyte (LLZTO) were used as a cathode electrolyte and an anode electrolyte, respectively. First, a 200-nm-thick Ag layer was coated on the LLZTO surface using a radio-frequency sputtering (SNTEK, 16-SN-055) with a Ag target (99.99%). The sputtering was performed for 500 s at 150 W at a working pressure of 5 mTorr under a 40-sccm flow of high-purity Ar gas (99.9999%) at a constant substrate temperature of 22°C.

As described elsewhere[23], an Ag–C layer coated on a 10-μm-thick SUS foil was prepared using a mixture of carbon black powder and Ag nanoparticles with 7 wt% of polyvinylidene fluoride. The Ag–C layer was attached as an anode interlayer on the acid-treated LLZTO surface via cold-isostatic pressing (CIP) under 250 MPa. After the SUS foil was peeled, a Li metal foil (20-μm-thick, Honjo Metal Co., Ltd.) was attached to the Ag–C surface via 250 MPa CIP. Commercially available $(Li_{1+x}(Ni_{0.33}Co_{0.33}Mn_{0.33})_{1-x}O_2$ (NCM, loading capacity: 3.2 g/cc, active material: 93 wt%; Samsung SDI) and $LiCoO_2$ (LCO, loading capacity: 4.22 g/cc, active material: 97.6 wt%; Samsung SDI) were employed as a cathode and Al foil was used as a current collector. An N-methyl-N-propyl pyrrolidinium bis(fluorosulfonyl)imide (Pyr13FSI, Kanto Chemical Co. Inc.) ionic liquid mixed with a 2 M lithium bis(fluorosulfonyl)imide (LiFSI) salt was used as the catholyte. The catholyte solution with 20wt% amount relative to the cathode was infiltrated into the cathode in a vacuum for 2 h. We put the ionic liquid-infiltrated cathode into the cathode side of the LLZTO in a pouch cell, and then sealed the cell under vacuum (750 Torr).

Characterization

Alternating current (AC)-impedance spectra were measured at 25°C with an open circuit in the potentiostatic mode over a frequency range from 0.1 Hz to 10 kHz using AC perturbation of 10 mV with a frequency response analyzer (Solartron, SI 1255 FRA) in conjunction with a potentiostat (Solartron, SI 1287 ECI). A battery cycler (Toscat-3100, Toyo System) was employed to measure the charge–discharge curves of the hybrid electrolyte cells at 25°C. The cells were cycled with a constant current (CC)-constant voltage (CV) charging and a CV discharging mode in the potential ranges of 2.8–4.3 and 2.8–4.5 V (vs. Li/Li^+) for NCM and LCO, respectively. We evaluated five cells of each sample to ensure data reliability.

We examined the cross-sectional microstructure of the interface between the anode and LLZTO electrolytes using an SU-8030 FE-SEM (Hitachi) coupled with an energy-dispersive X-ray spectroscopy (EDS) spectrometer with an accelerating voltage of 5 kV and a working distance of 8 mm.

The adhesion strength between LLZTO and the interlayer was evaluated by measuring the peel strength using a tensile strength tester (AGS-X, Shimadzu). The anode interlayer was attached on the acid-treated surface of the LLZTO by CIP under 250 MPa, and the peel strength was measured by pulling the SUS foil at a cross-head speed of 100 mm/min.

Computational details

All density functional theory (DFT) calculations were conducted using Vienna Ab initio Simulation Package (VASP)[24]. Exchange-correlation energies were dealt with spin-polarized generalized gradient approximation parameterized by Perdew-Burke-Ernzerhof[25]. We used projector-augmented wave pseudopotentials with a plane-wave basis set as implemented in VASP[26]. To describe van der Waals interaction, DFT-D3 dispersion correction proposed by Grimme *et al.* was applied, except for metallic structures[27]. A kinetic energy cutoff of 400 eV was used for all calculations involving slab geometry, and structure optimization was performed until the remaining forces converged within 0.02 eV/Å.

Interface models with sufficiently thick (> 15 Å) vacuum slabs were constructed to describe various interfaces in LMBs. To generate interfaces between two different materials, most stable surfaces were first identified for each material. In particular, the (100) surface with a Zr-poor configuration was used for LLZTO following the work of Canepa *et al.*[28], and (111) surface was selected for Fe, Cu and Ag. In addition, (100) and (001) surfaces were used for Li and graphite, respectively. Then, we cleaved bulk structures to form two surface slab models. Here, convergence tests were performed to determine the thicknesses of slabs. Finally, interfaces were formed by aligning two surface slabs. Because of the different lattice parameters of slab models, we allowed slight angle distortion (< 3°) and/or elongation or shrinkage of lattice (< 5%) to ensure the lattice compatibility. All interface building processes were performed using the *pymatgen* python package[29].

Structural relaxation of interfaces was conducted in two steps: distance between two surfaces was first optimized; then, one of the surface structures was laterally shifted to determine the most stable alignment between two surface structures. The adhesion energy (W_{ad}) was obtained by comparing the energies of interface structure and isolated surface structures.

$$W_{ad} = \frac{1}{A}\left(E_{interface} - E_{substrate} - E_{film}\right), \quad (1)$$

where A is the area of interface. $E_{interface}$, $E_{substrate}$, and E_{film} are calculated energies of interface, substrate, and film structures, respectively.

Results

Role of interlayer to regulate Li deposition site

The key role of the interlayer is to induce Li plating away from the solid electrolyte, preventing direct contact between Li metal and the solid electrolyte and suppressing dendrite penetration. Recent studies using sulfide electrolyte suggested that carbon-based layer serve this purpose, but a fundamental understanding of this mechanism remains lacking[23]. Therefore, before implementing carbon-based composite onto LLZTO, we attempted to elucidate the Li deposition behavior in the presence of interlayer and determine whether carbon-based interlayer could regulate the Li deposition site in contact with LLZTO.

Figure 1a and 1b illustrate two possible scenarios of Li deposition during charging. Li can either be deposited between the solid electrolyte and interlayer, or between the interlayer and current collector. Without an additional driving force, Li^+ transported from the solid electrolyte should be reduced and plated between the solid electrolyte and interlayer (Fig. 1a) because of the electron-ion mixed-conducting nature of the carbon-based interlayer. However, to the contrary, it was observed that Li deposition occurs at the interface between the current collector and interlayer (Fig. 1b)[23]. This indicates that the reduced Li moved through the interlayer and is plated near the current collector. To understand the driving force behind this Li transport, we conducted DFT calculation to assess the thermodynamically favorable site for Li deposition.

As shown in Fig. 1a and 1b, the internal arrangement of cell components after charging varies with the Li plating site, leading to a distinct interface for each configuration. Therefore, by comparing total interface energies, we could predict the thermodynamically favorable Li deposition site. To assess the interface energies, atomic models were built for each interface, as shown in Fig. 1c, for the LLZTO/Li interface, and the work of adhesion (W_{ad}) was calculated accordingly (refer to Computational Details section for interface modeling process). Using graphite as an interlayer and Cu or Fe (representing SUS) as a current collector, our DFT calculations suggest that the latter case (Fig. 1b) is the more favorable state by ~ 0.51 J/m^2 and ~ 0.98 J/m^2, respectively. Notably, using the Li_6PS_5Cl solid electrolyte results in an identical trend (favorable deposition at the Cu current collector side by ~ 0.2 J/m^2), corroborating the recent experimental observation[23]. This indicates that the thermodynamically favorable Li deposition site is between the current collector and interlayer, unless there is no kinetic barrier for Li transport through the interlayer. If the time for Li to move toward the current collector through the interlayer is insufficient, Li is undesirably plated near the solid electrolyte, although it is thermodynamically unfavorable. In other words, Li transport through the interlayer should be faster than Li influx from the cathode side, which is dependent on the charge rate. Therefore, it is crucial to enhance Li transport kinetics. Notably, the above discussion is valid for the ideal interfacial contact; any imperfections that may occur in real cases could lead to different outcomes.

These results demonstrate that the use of carbon-based interlayer could ultimately protect the LLZTO/Li interface, if the cell is carefully fabricated and cycled under optimal conditions. Encouraged by this understanding, we attempted to employ a Ag–C interlayer onto LLZTO to prevent direct contact between Li and LLZTO. For proof-of-concept, we fabricated a cell with the Ag–C composite attached to a thick

LLZTO pellet (~ 350-μm-thick) and examined the Li deposition site after charging (see Experimental details for the fabrication process). As expected, SEM observations (Fig. 2) show that Li truly penetrates the Ag–C interlayer and is plated between the Ag–C interlayer and current collector, indicating that the interlayer strategy could be successfully employed with garnet-type oxide solid electrolytes.

Integration of Ag–C composite onto thin tape-cast LLZTO

In the previous section, we demonstrated that the Ag–C interlayer can effectively regulate the Li deposition site. Moreover, to realize competitive energy density in a cell level, we attempted to integrate a Ag–C composite onto thin (< 100 μm) tape-cast LLZTO. However, we observed that the clean transfer of the Ag–C interlayer onto ~ 100-μm-thick tape-cast LLZTO was challenging in some cases, and the transfer process is unreliable. As shown in Fig. 3a, a portion of Ag–C (black) was often not attached to LLZTO (light pink), resulting in a messy and inhomogeneous surface. Even after CIP, we frequently observed the partial detachment of the interlayer. We observed that the adhesion between carbon and LLZTO is weak. DFT calculation results demonstrate that W_{ad} between LLZTO and carbon is − 0.33 J/m^2, which is lower than that of the LLZTO/Li interface (− 0.71 J/m^2). Applying significantly higher pressure could be an effective approach for ductile sulfide solid electrolytes or robust thick oxide pellets to enhance adhesion, where the solid electrolyte and Ag–C can withstand high stress. However, thin LLZTO tape is highly brittle; therefore, it is imperative to determine an alternative method to enhance the adhesion between LLZTO and Ag–C composite.

To achieve a well-attached interface between the interlayer and solid electrolyte, we attempted to introduce an additional layer serving as an adhesive agent at the interface. Additional to binding, this layer requires possessing the following characteristics. First, it should not hinder Li diffusion during charge and discharge, because slow Li diffusion might result in Li plating between the solid electrolyte and interlayer. It should also be chemically or electrochemically stable with LLZTO and the Ag–C interlayer. Considering these criteria, we decided to employ Ag, which was recently demonstrated to facilitate Li nucleation and enable fast Li diffusion in Li–Ag alloys[17,30].

Next, we investigated whether Ag could enhance the adhesion between LLZTO and the Ag–C composite. Our DFT calculations indicated that the adhesion between the interlayer and the solid electrolyte could be enhanced with the Ag layer. As previously noted, W_{ad} between graphite and LLZTO is − 0.33 J/m^2 (Fig. 3c), but Ag provides a more favorable interface with both LLZTO and graphite. Calculated work of adhesions between LLZTO and Ag, and that between Ag and graphite are − 0.80 and − 0.56 J/m^2, respectively (Fig. 3d).

To experimentally demonstrate the effect of Ag, we introduced a ~ 200-nm-thick Ag layer by sputtering onto tape-cast LLZTO. Then, we transferred a Ag–C composite onto the Ag-coated LLZTO. In line with theoretical prediction, we visually observed a uniform transfer of interlayer to LLZTO (Fig. 3b). Compared with the Ag–C transfer to pristine LLZTO tape (Fig. 3a), a sharp difference is shown, indicating that Ag successfully binds LLZTO and Ag–C composite. Enhanced adhesion was further quantified by the peel-

off test, as shown in Fig. 3e. Peel strength between LLZTO and Ag–C interlayer is ~ 10 mN/mm without the Ag layer, but it increases to ~ 180 mN/mm after Ag layer introduction, demonstrating the increase in interface adhesion.

The increased binding strength between Ag and LLZTO is attributable to the increased electronic interaction. To examine charge distribution behavior at the interface, we performed differential charge density analysis.

$$\rho_{diff} = \rho_{interface} - \rho_{substrate} - \rho_{film}$$

2

,

where ρ_{diff} is the redistributed charge density upon the formation of interface, while $\rho_{interface}$, $\rho_{substrate}$, and ρ_{film} are the charge densities of the interface, substrate, and film structures, respectively. According to ρ_{diff} at LLZTO/Ag and LLZTO/graphite interfaces, a larger amount of charge is evidently transferred at the LLZTO/Ag interface (Fig. S1), which may be responsible for the enhanced adhesion. These results indicate that Ag could successfully aid the binding between LLZTO and Ag–C interlayer owing to the increased electronic interaction.

Full cell assembly and electrochemical characterization

Having confirmed that the Ag layer can enhance interfacial binding, we fabricated a hybrid cell with a Ag layer and Ag–C interlayer to investigate the electrochemical performance. Electrochemical cells were assembled with both a thick LLZTO pellet (~ 350 μm) and thin LLZTO tape (< 100 μm). Figure 4a shows the schematics of cell configuration fabricated with a LLZTO pellet. For the hybrid cell, Li metal was initially placed at the anode to promote Li nucleation, and an ionic liquid was used at the cathode for enhanced interface wetting and utilization. As shown in Fig. 4b, no significant capacity degradation and short-circuiting is observed at the 0.5 C-rate (1.6 mA/cm^2) operation. Notably, no external pressure was applied, and the cell was operated at room temperature. The SEM image and EDS data (Fig. 4c) show that Ag remained in the layer form even after 100th cycle at the carbon-LLZTO interface, although some Ag particles were observed to be distributed in the Li metal owing to their thermodynamic preference for the formation of Li–Ag alloy during cycling[23,30]. As expected from theoretical results, this indicates that reversible Li deposition and stripping occurred between the interlayer and current collector, preventing contact between Li and LLZTO. In addition, it demonstrates that the interface between the anode interlayer and current collector remained intact for long cycles.

To elucidate the effect of Ag interlayer on the electrochemical performance using LLZTO tape, we fabricated a coin-sized hybrid cell comprising an 80-μm tape and a 3.2-mAh/cm^2 NCM cathode, as shown in Fig. 5a. Because the predominant issue for utilizing the LLZTO tape was the contact between LLZTO and the Ag–C interlayer (Fig. 3a, 3b), we measured the AC impedance spectra to investigate the change in interfacial resistance. The Nyquist plot of the impedance spectra (Fig. 5b) shows that the

Ohmic losses are virtually identical for the both cells, whereas the high-frequency arc associated with the charge-transfer reactions at the cathode–anode interfaces decreases significantly when Ag is present on the LLZTO surface. Assuming that the cathode interfacial kinetics is unchanged in the presence of Ag, the decrease in the high-frequency arc is attributable to the improved charge-transfer kinetics at the anode-LLZTO interface due to the increased effective area and the enhanced bonding of anode to LLZTO.

Accordingly, the charging/discharging curve (Fig. 5c, d) shows that the hybrid cell without Ag failed at a current density of 1 mA/cm^2 by short-circuiting, while the cell with the Ag layer was capable of operating at a high current density of 1.6 mA/cm^2 without short-circuiting. Owing to the adhesion of Ag, our interlayer could successfully protect LLZTO from dendrite penetration, which helped realize a high volumetric energy density and an excellent long-term cycle stability for 800 cycles (Fig. 5e). Considering that our cell was operated at room temperature without external pressure, these results pave the way for the use of LMBs in various fields, such as in mobile and wearable devices, that require low-temperature operation and limited volume. Additionally, this type of cell can potentially deliver a considerable energy density of 680 Wh/L assuming our hybrid battery configuration as one-unit cell in pack, which is promising for practical applications.

We also examined the hybrid cell with a 3.2-mAh/cm^2 LCO cathode and large-area thin tape electrolyte (area 2.53 cm × 2.53 cm, thickness 80 μm) under a high charging voltage cutoff of 4.5 V (vs. Li/Li$^+$) to demonstrate its applicability in more practical condition. As shown in Fig. 6a, the larger area cathode was used in this cell and the 12-mA-capacity cell was tested at room temperature. The charging–discharging curves of Fig. 6b show that the cell delivers the designed capacity of ~ 3.2 mAh/cm^2 at 0.64 mA/cm^2 under the condition of 4.5 V cutoff. The nominal voltage of the cell at 1 mA/cm^2 is calculated to be 3.93 V (vs. Li/Li$^+$), which meets the working voltage range required for commercial smartphone batteries. Figure 6c shows a stable cycling performance over 150 cycles without significant capacity decay or short-circuit signal at a constant current density of 1 mA/cm^2, which agrees well with that of the NCM-Li cell shown in Fig. 5e.

We believe that our careful interlayer design is attributable to the exceptional performance of solid-state batteries. We demonstrated excellent lifespan of over 800 cycles at 25°C without external pressure, which could meet the cycling requirements and the operating conditions of smartphone batteries, which are represented by: (i) 400 cycles @88% cycle retention without Li metal shorting at the operating current density of 1.6 mA/cm^2 (0.5 C-rate charging/discharging) and (ii) room-temperature operation under the condition of no external pressure. To the best of our knowledge, these commercial-level performances at 25°C is the first reported in Li metal batteries employing a solid oxide electrolyte, as described in Fig. 7[31–46].

Discussion

Electrochemical reaction in a battery takes place at the interface between an electrolyte and an electrode. Since carbon is conductive, our carbon-based interlayer could be regarded as an electrode. Therefore, if we employ carbon black as an anode interlayer, a redox reaction would take place at the interface between a solid electrolyte and the interlayer. Li ion transported from the electrolyte during charge is expected to be reduced to Li metal as carbon black is unable to host Li ion intercalation. If Li stays at this interface, the interlayer could not prevent the dendrite penetration since Li would grow near solid electrolyte. However, we demonstrated that Li could actually be plated at the interface between the interlayer and the current collector. Given that the reduction reaction occurs at the electrolyte/interlayer interface, this indicates that Li metal was transported from the solid electrolyte/interlayer interface toward interlayer/current collector interface. Through theoretical calculation of interface adhesion energies, we suggested Li stability difference at each interface as possible driving force for Li transportation (Fig. 1a and 1b). To ensure the current collector side deposition, interface adhesion between the current collector and interlayer should be weak, and that between the interlayer and solid electrolyte should be strong.

It is widely reported that creep is a major mechanism for Li deformation[47–49], since the homologous temperature of Li metal at room temperature is as high as 0.66. As Li reduction constantly takes place at the electrolyte/interlayer interface during charge, stress is consistently generated at the interface. After Li fully fills the pores and void spaces in interlayer, this stress drives Li extrusion toward the current collector. In this way, the solid electrolyte could be protected from dendrite penetration originating from irregular Li growth near the surface. During discharge, the overall process is reversed. Li metal near the solid electrolyte is first oxidized to Li ion, forming Li vacancy. Then, Li metal would be deformed to fill the vacancy. During the whole charge and discharge process, solid electrolyte keeps interface with carbon-based interlayer, avoiding the harsh mechanical stress from abrupt morphology evolution during Li plating and stripping. Under this mechanism, increasing the charge current density would result in fast Li accumulation at the solid electrolyte/interlayer interface, which leads to the severe stress buildup. Therefore, to warrant cycle stability under high current density, Li transport through the interlayer should be fast enough to quickly relieve the stress, and the adhesion between the solid electrolyte and interlayer should be strong enough to endure the local stress. We believe that careful design of interlayer morphology with optimized microstructure, pore structure and tortuosity could enhance the Li transport kinetics through the interlayer.

In summary, all-solid-state Li metal batteries were prepared using a Ag-coated LLZTO, Ag–C composite interlayer, and NCM cathode. Theoretical calculations demonstrated that carbon-based interlayer could regulate the Li deposition towards the current collector side, preventing the direct contact of Li and LLZTO and effectively suppress dendrite penetration. Sputtered Ag layer was applied to enhance the adhesion between LLZTO and the interlayer. Owing to our careful design, the prototype cell exhibited a high energy density (~ 680 Wh/L) for over 800 cycles at room temperature without applying external pressure. We believe our results provide valuable insights into the advancement of the field of LMBs, and toward the realization of practical LMB operation.

References

1. Krauskopf, T., Richter, F. H., Zeier, W. G. & Janek, J. Physicochemical Concepts of the Lithium Metal Anode in Solid-State Batteries. Chem. Rev. **120**, 7745–7794 (2020).
2. Manthiram, A., Yu, X. & Wang, S. Lithium battery chemistries enabled by solid-state electrolytes. Nat. Rev. Mater. **2**, 1–16 (2017).
3. Zhao, Q., Stalin, S., Zhao, C.-Z. & Archer, L. A. Designing solid-state electrolytes for safe, energy-dense batteries. Nat. Rev. Mater. **5**, 229–252 (2020).
4. Famprikis, T., Canepa, P., Dawson, J. A., Islam, M. S. & Masquelier, C. Fundamentals of inorganic solid-state electrolytes for batteries. Nat. Mater. **18**, 1278–1291 (2019).
5. Murugan, R., Thangadurai, V. & Weppner, W. Fast Lithium Ion Conduction in Garnet-Type Li7La3Zr2O12. Angew. Chem. Int. Ed. **46**, 7778–7781 (2007).
6. Zhao, N. *et al.* Solid Garnet Batteries. Joule **3**, 1190–1199 (2019).
7. Jalem, R. *et al.* Concerted Migration Mechanism in the Li Ion Dynamics of Garnet-Type Li7La3Zr2O12. Chem. Mater. **25**, 425–430 (2013).
8. Samson, A. J., Hofstetter, K., Bag, S. & Thangadurai, V. A bird's-eye view of Li-stuffed garnet-type Li7La3Zr2O12 ceramic electrolytes for advanced all-solid-state Li batteries. Energy Environ. Sci. **12**, 2957–2975 (2019).
9. Miara, L. J., Richards, W. D., Wang, Y. E. & Ceder, G. First-Principles Studies on Cation Dopants and Electrolyte|Cathode Interphases for Lithium Garnets. Chem. Mater. **27**, 4040–4047 (2015).
10. Meier, K., Laino, T. & Curioni, A. Solid-State Electrolytes: Revealing the Mechanisms of Li-Ion Conduction in Tetragonal and Cubic LLZO by First-Principles Calculations. J. Phys. Chem. C **118**, 6668–6679 (2014).
11. Krauskopf, T., Mogwitz, B., Rosenbach, C., Zeier, W. G. & Janek, J. Diffusion Limitation of Lithium Metal and Li–Mg Alloy Anodes on LLZO Type Solid Electrolytes as a Function of Temperature and Pressure. Adv. Energy Mater. **9**, 1902568 (2019).
12. Krauskopf, T. *et al.* The Fast Charge Transfer Kinetics of the Lithium Metal Anode on the Garnet-Type Solid Electrolyte Li6.25Al0.25La3Zr2O12. Adv. Energy Mater. **10**, 2000945 (2020).
13. Kasemchainan, J. *et al.* Critical stripping current leads to dendrite formation on plating in lithium anode solid electrolyte cells. Nat. Mater. **18**, 1105–1111 (2019).
14. Ning, Z. *et al.* Visualizing plating-induced cracking in lithium-anode solid-electrolyte cells. Nat. Mater. **20**, 1121–1129 (2021).
15. Ping, W. *et al.* Reversible Short-Circuit Behaviors in Garnet-Based Solid-State Batteries. Adv. Energy Mater. **10**, 2000702 (2020).
16. Xu, H. *et al.* Li3N-Modified Garnet Electrolyte for All-Solid-State Lithium Metal Batteries Operated at 40°C. Nano Lett. **18**, 7414–7418 (2018).

17. Kim, S. *et al.* The Role of Interlayer Chemistry in Li-Metal Growth through a Garnet-Type Solid Electrolyte. Adv. Energy Mater. **10**, 1903993 (2020).
18. Chen, Y. *et al.* Nanocomposite intermediate layers formed by conversion reaction of SnO2 for Li/garnet/Li cycle stability. J. Power Sources **420**, 15–21 (2019).
19. Shi, K. *et al.* In Situ Construction of an Ultra-Stable Conductive Composite Interface for High-Voltage All-Solid-State Lithium Metal Batteries. Angew. Chem. Int. Ed. **59**, 11784–11788 (2020).
20. Huo, H. *et al.* A flexible electron-blocking interfacial shield for dendrite-free solid lithium metal batteries. Nat. Commun. **12**, 176 (2021).
21. Hitz, G. T. *et al.* High-rate lithium cycling in a scalable trilayer Li-garnet-electrolyte architecture. Mater. Today **22**, 50–57 (2019).
22. Kim, S. *et al.* High-energy and durable lithium metal batteries using garnet-type solid electrolytes with tailored lithium-metal compatibility. Nat. Commun. **13**, 1883 (2022).
23. Lee, Y.-G. *et al.* High-energy long-cycling all-solid-state lithium metal batteries enabled by silver–carbon composite anodes. Nat. Energy **5**, 299–308 (2020).
24. Kresse, G. & Furthmüller, J. Efficient iterative schemes for ab initio total-energy calculations using a plane-wave basis set. Phys. Rev. B **54**, 11169–11186 (1996).
25. Perdew, J. P., Burke, K. & Ernzerhof, M. Generalized Gradient Approximation Made Simple. Phys. Rev. Lett. **77**, 3865–3868 (1996).
26. Blöchl, P. E. Projector augmented-wave method. Phys. Rev. B **50**, 17953–17979 (1994).
27. Grimme, S., Ehrlich, S. & Goerigk, L. Effect of the damping function in dispersion corrected density functional theory. J. Comput. Chem. **32**, 1456–1465 (2011).
28. Canepa, P. *et al.* Particle Morphology and Lithium Segregation to Surfaces of the Li7La3Zr2O12 Solid Electrolyte. Chem. Mater. **30**, 3019–3027 (2018).
29. Ong, S. P. *et al.* Python Materials Genomics (pymatgen): A robust, open-source python library for materials analysis. Comput. Mater. Sci. **68**, 314–319 (2013).
30. Jin, S. *et al.* Solid–Solution-Based Metal Alloy Phase for Highly Reversible Lithium Metal Anode. J. Am. Chem. Soc. **142**, 8818–8826 (2020).
31. Han, F. *et al.* Interphase Engineering Enabled All-Ceramic Lithium Battery. Joule **2**, 497–508 (2018).
32. Shao, Y. *et al.* Drawing a Soft Interface: An Effective Interfacial Modification Strategy for Garnet-Type Solid-State Li Batteries. ACS Energy Lett. **3**, 1212–1218 (2018).
33. Luo, W. *et al.* Reducing Interfacial Resistance between Garnet-Structured Solid-State Electrolyte and Li-Metal Anode by a Germanium Layer. Adv. Mater. **29**, 1606042 (2017).
34. Ohta, S., Kobayashi, T., Seki, J. & Asaoka, T. Electrochemical performance of an all-solid-state lithium ion battery with garnet-type oxide electrolyte. J. Power Sources **202**, 332–335 (2012).
35. Chen, S. *et al.* All-Solid-State Batteries with a Limited Lithium Metal Anode at Room Temperature using a Garnet-Based Electrolyte. Adv. Mater. **33**, 2002325 (2021).

36. Liu, B. *et al.* Garnet Solid Electrolyte Protected Li-Metal Batteries. ACS Appl. Mater. Interfaces **9**, 18809–18815 (2017).
37. Ruan, Y. *et al.* A 3D Cross-Linking Lithiophilic and Electronically Insulating Interfacial Engineering for Garnet-Type Solid-State Lithium Batteries. Adv. Funct. Mater. **31**, 2007815 (2021).
38. Chen, C. *et al.* Sustainable Interfaces between Si Anodes and Garnet Electrolytes for Room-Temperature Solid-State Batteries. ACS Appl. Mater. Interfaces **10**, 2185–2190 (2018).
39. Lan, W. *et al.* Realizing Li7La3Zr2O12 garnets with high Li + conductivity and dense microstructures by Ga/Nb dual substitution for lithium solid-state battery applications. Sustain. Energy Fuels **4**, 1812–1821 (2020).
40. Tian, Y. *et al.* Li6.75La3Zr1.75Ta0.25O12@amorphous Li3OCl composite electrolyte for solid state lithium-metal batteries. Energy Storage Mater. **14**, 49–57 (2018).
41. Zhang, J., Li, J., Zhai, H., Tan, G. & Tang, X. One-Step Processing of Soft Electrolyte/Metallic Lithium Interface for High-Performance Solid-State Lithium Batteries. ACS Appl. Energy Mater. **3**, 6139–6145 (2020).
42. Dubey, R. *et al.* Building a Better Li-Garnet Solid Electrolyte/Metallic Li Interface with Antimony. Adv. Energy Mater. **11**, 2102086 (2021).
43. Yang, L. *et al.* Efficient Mutual-Compensating Li-Loss Strategy toward Highly Conductive Garnet Ceramics for Li-Metal Solid-State Batteries. ACS Appl. Mater. Interfaces **13**, 56054–56063 (2021).
44. Fu, K. (Kelvin) *et al.* Toward garnet electrolyte–based Li metal batteries: An ultrathin, highly effective, artificial solid-state electrolyte/metallic Li interface. *Sci. Adv.* **3**, e1601659 (2017).
45. Li, X. *et al.* Rational design of strontium antimony co-doped Li7La3Zr2O12 electrolyte membrane for solid-state lithium batteries. J. Alloys Compd. **794**, 347–357 (2019).
46. Huo, H. *et al.* In-situ formed Li2CO3-free garnet/Li interface by rapid acid treatment for dendrite-free solid-state batteries. Nano Energy **61**, 119–125 (2019).
47. Chen, Y. *et al.* Li metal deposition and stripping in a solid-state battery via Coble creep. Nature **578**, 251–255 (2020).
48. Wang, Z. *et al.* Creep-Enabled 3D Solid-State Lithium-Metal Battery. Chem **6**, 2878–2892 (2020).
49. LePage, W. S. *et al.* Lithium Mechanics: Roles of Strain Rate and Temperature and Implications for Lithium Metal Batteries. J. Electrochem. Soc. **166**, A89 (2019).

Declarations

Acknowledgements

This work was supported by funds from Samsung Electronics Co. Ltd.

Author contributions

J.-S. K. and G.Y. conceived and designed the overall experiments, analyzed the data, and wrote the manuscript. J.-S. K. and S. K. performed all electrochemical experiments. G.Y. performed DFT calculations on the adhesion energies of the anode-solid electrolyte interfaces. S. S., N. Y and S. S. prepared the Ag–C anode interlayer and measured peel strength between the LLZTO and the Ag–C interlayer. All the authors participated in discussion and provided constructive advice for experimental design.

Competing interests

The authors declare no competing interests.

Materials & Correspondence

*Ju-Sik Kim: jusik.kim@samsung.com

*Dongmin Im: dongmin.im@samsung.com

Data and materials availability

All data is available in the main text or the supplementary materials.

Figures

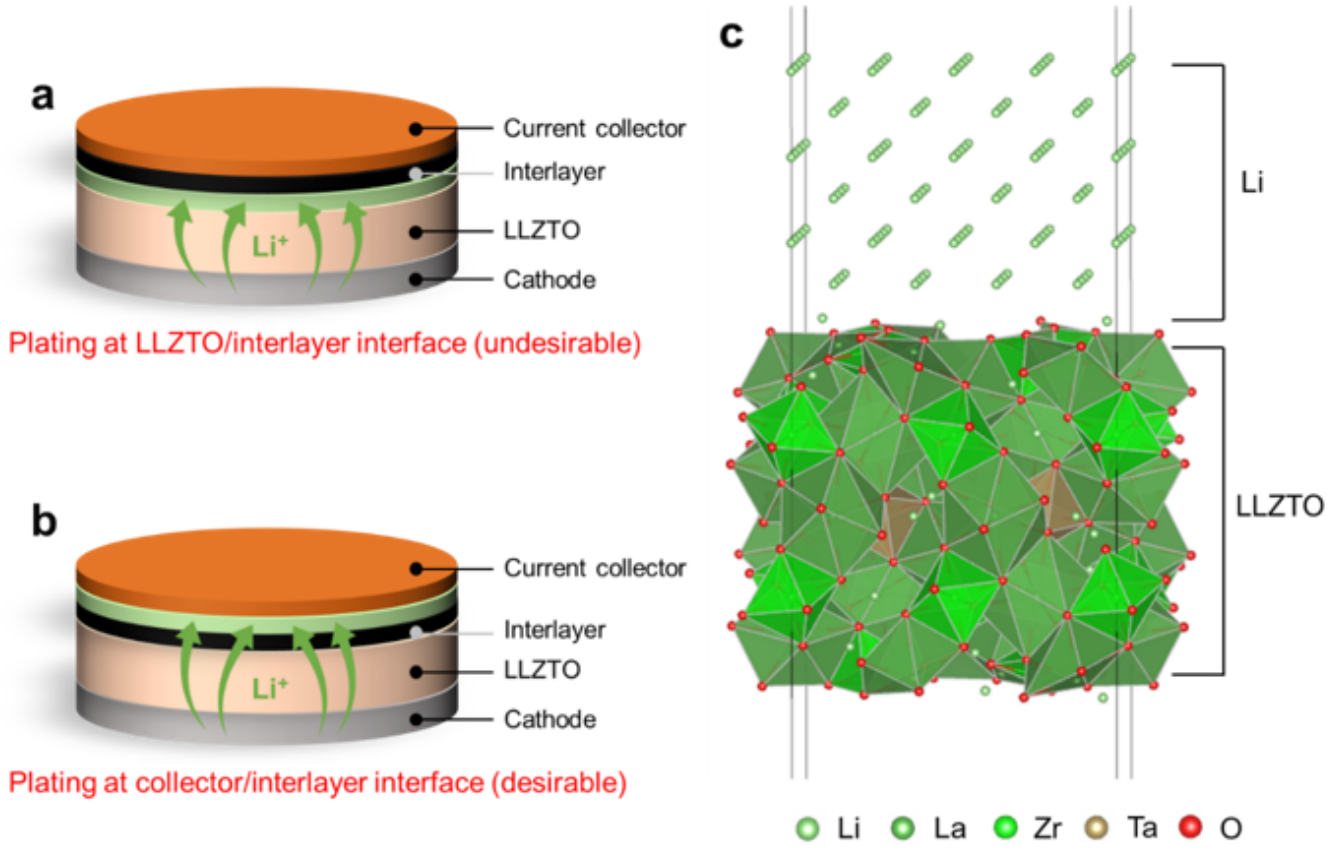

Figure 1

(a, b) Two scenarios of Li deposition in LMBs with interlayer. (a) LLZTO side plating, (b) current collector side plating. (c) Atomic model of LLZTO/Li interface.

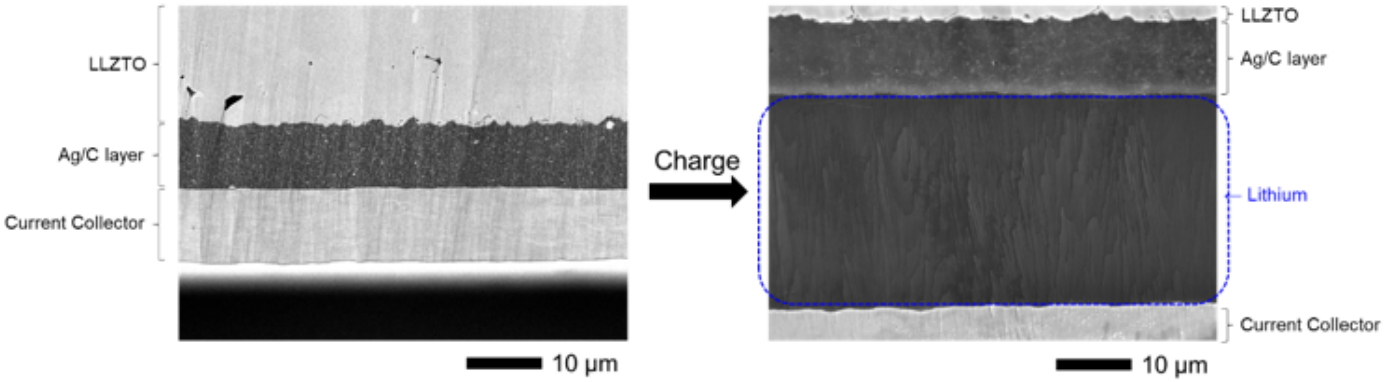

Figure 2

Cross-section SEM image of the cell before and after lithiation, where current collector side plating is distinctly observed.

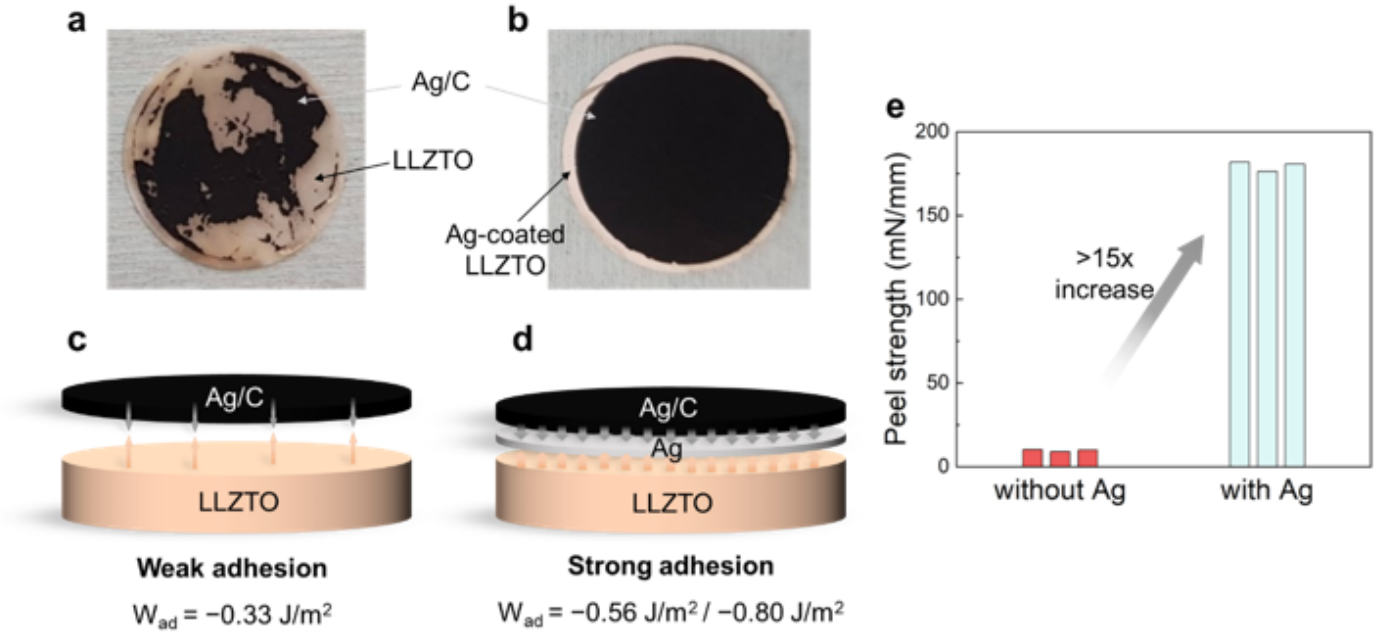

Figure 3

Optical image of LLZTO after the transfer of Ag–C interlayer (a) without and (b) with Ag coating layer. Schematic models of LLZTO/interlayer interface (c) without and (d) with Ag layer, illustrating the role of Ag as a binding agent. (e) Measured peel strength between LLZTO and Ag–C interlayer.

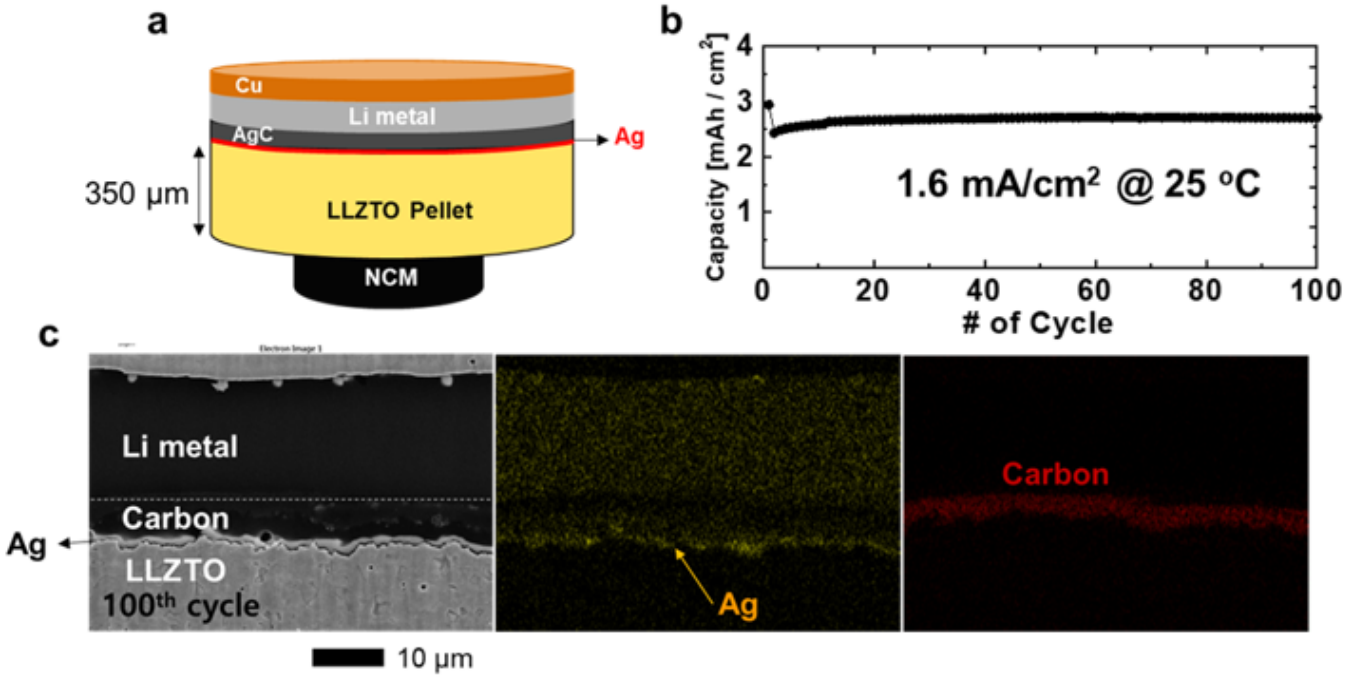

Figure 4

(a) Schematic of assembled cell using LLZTO pellet. (b) Cycling performance of NCM (3.2 mAh/cm^2)/LLZTO/Ag/AgC/Li cell. (c) Cross-section SEM image and elemental analysis of the cell after 100 cycles.

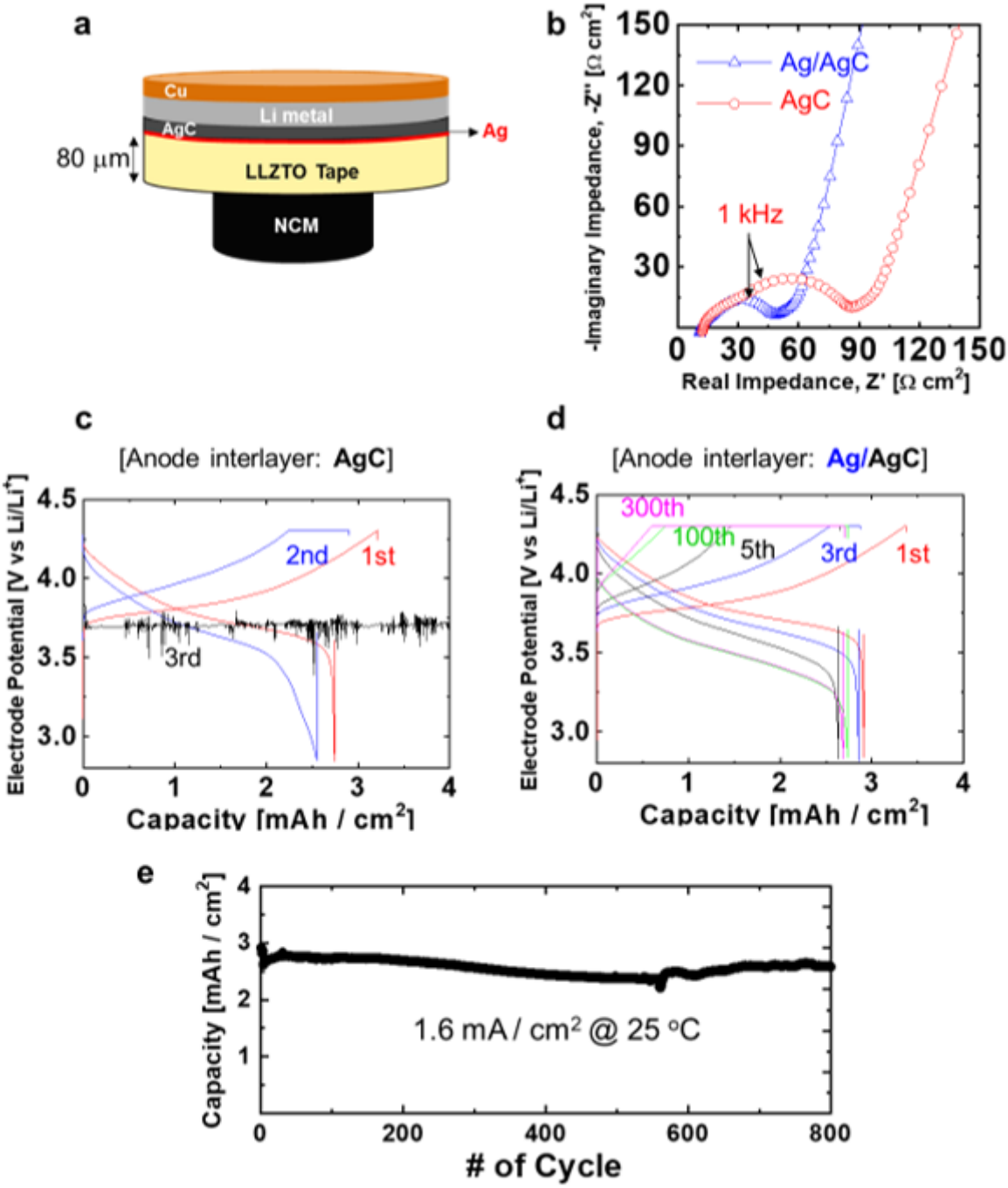

Figure 5

(a) Schematic picture of the assembled cell using LLZTO tape. (b) Nyquist plots of AC-impedance spectra obtained from the hybrid electrolyte cells. Galvanostatic voltage profiles of the hybrid electrolyte NCM-Li full cells with (c) AgC and (d) Ag/AgC anode interlayer. (e) Cycling performance of NCM(3.2 mAh/cm^2)/LLZTO/Ag/AgC/Li cell.

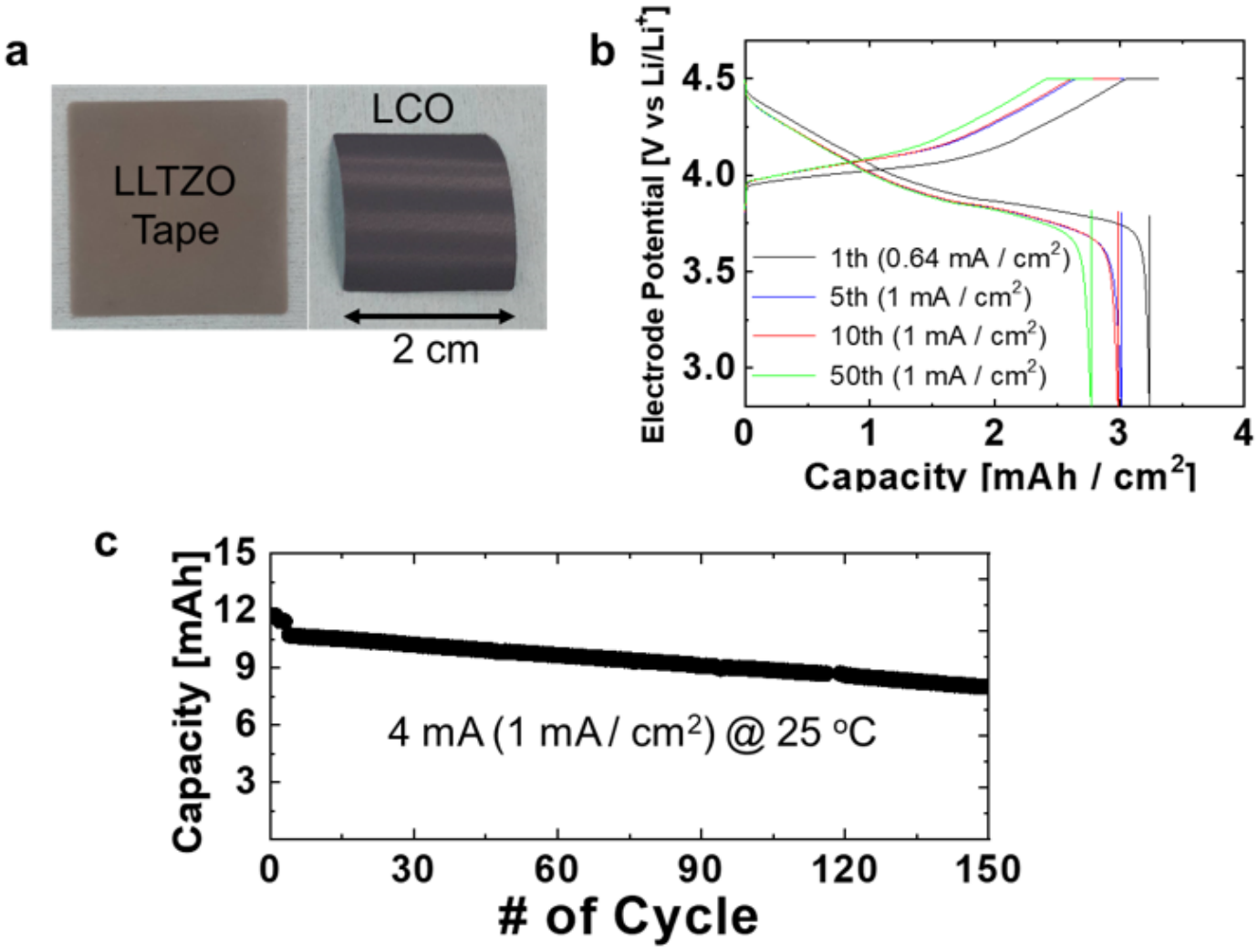

Figure 6

(a) LLZTO tape (2.53 cm × 2.53 cm, 80 mm) and LCO (2 cm × 2 cm). (b) Galvanostatic voltage profiles of the hybrid electrolyte LCO-Li full cells with Ag/AgC anode interlayer. (c) Cycling performance of LCO/LLZTO/Ag/AgC/Li cell at 25 °C without external pressure.

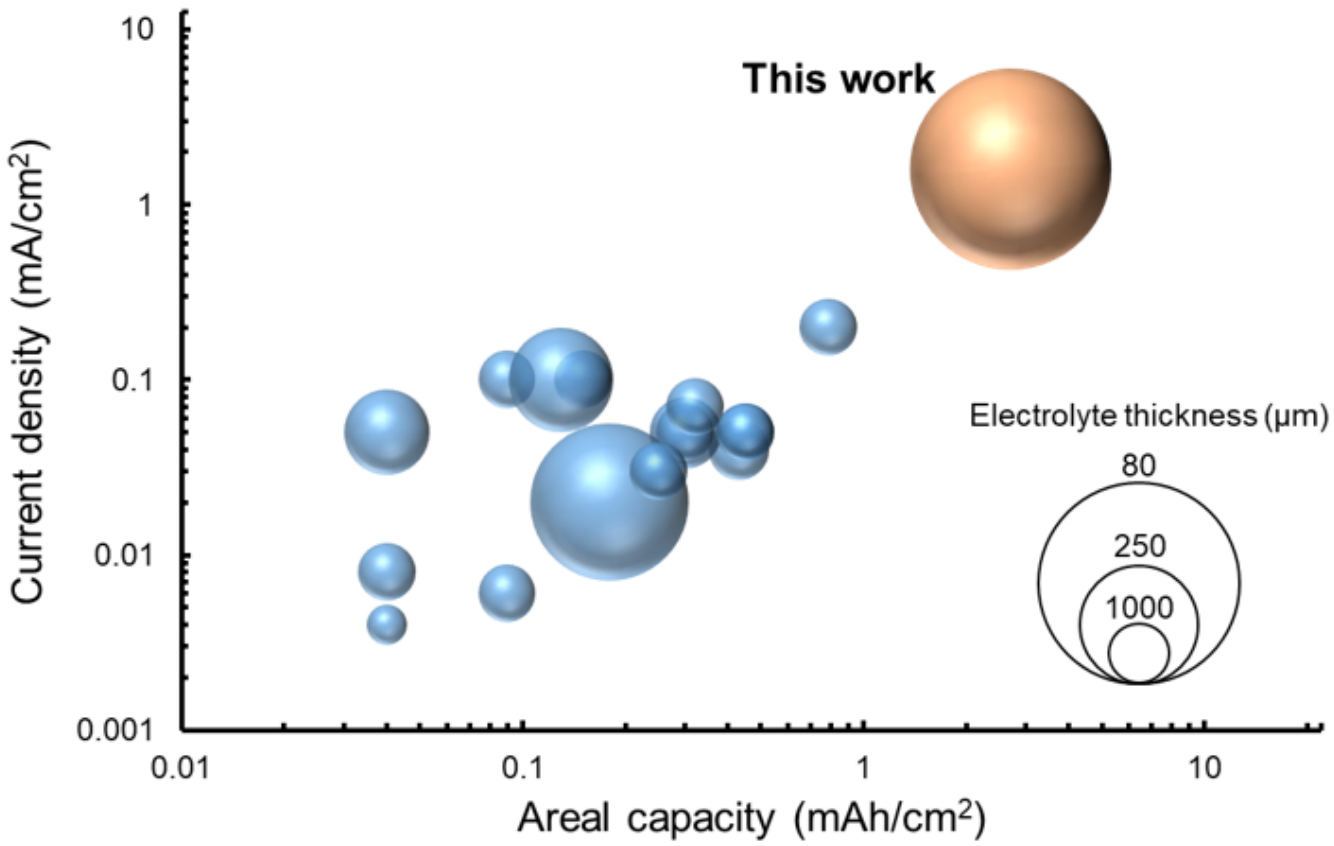

Figure 7

Summary of areal capacity and operating current density of reported LLZO-based batteries. Full-cells which are reversibly cycled for at least 100 times at room temperature are presented. More details including cell configuration, number of reversible cycles are summarized in Table S1.

Supplementary Files

This is a list of supplementary files associated with this preprint. Click to download.

- SupplementaryInformation220408editted.docx